Journal of Membrane Science, 77 (1993) 1-22
Elsevier Science Publishers B.V., Amsterdam

Diagnosis of membrane fouling using a rotating annular filter. 1.
Cell culture media

Georges Belfort[a], Joseph M. Pimbley[b], Anthony Greiner[a] and Kun Yong Chung[a,*]
[a]*Bioseparations Research Center, Howard P. Isermann Department of Chemical Engineering, Rensselaer Polytechnic Institute, Troy, NY 12180-3590 (USA)*
[b]*Department of Mathematical Sciences, Rensselaer Polytechnic Institute, Troy, NY 12180-3590 (USA)*

(Received February 6, 1992; accepted in revised form June 8, 1992)

Abstract

Membrane fouling is dissected into pore narrowing and constriction, pore plugging and deposition of a gel/cake onto the upstream face of a membrane. Using a rotating annular membrane filter as a diagnostic tool, we have identified these fouling components with the aid of pemeation flux-transmembrane pressure plots. The choice of the rotating annular filter is of particular significance since the transmembrane pressure is decoupled from axial flow in this system. The Navier-Stokes equations for azimuthal flow in an annulus with a porous wall on the rotating inner cylinder is solved for the narrow-gap approximation and with several other reasonable simplifications. This solution is used to analyse the data by plotting the flux versus the actual transmembrane pressure and accounting for the centrifugal pressure. Universal plots for all rotational speeds are observed for deionized water and for fouling solutions containing interacting solutes that are relatively small compared to the mean pore size of the membrane. Pore narrowing, constriction and plugging are the dominant forms of fouling in this case. This type of fouling manifests itself in the flux-pressure diagram as a decrease in the slope of a linear plot. We model these effects with the help of the approach of Meireles et al. [J. Membrane Sci. 56 (1991) 13] and correct and extend their formalism with explicit solutions. One such explicit solution for the ratio of the flux-pressure slopes is particularly useful for estimating the number of adsorbed monolayers of a molecule of known dimensions. Without a detailed understanding of solute deposition on the membrane upstream face and its effect on the flux versus transmembrane pressure, we invoke a phenomenological approach to obtain a useful model for describing this phenomenon as a function of rotational speed. This approach is appropriate for solutions containing solutes or their aggregates that are relatively large compared to the mean pore size of the membrane. Surface deposition onto the upstream face of the membrane is the dominant mechanism of fouling. This type of fouling manifests itself in the flux-pressure diagram as a continously decreasing slope or convex Langmuir-like profile. The approach assumes that the resistance to flow through the gel/cake is dependent on transmembrane pressure and inversely dependent on rotational speed. In summary, transmembrane pressure is used to (i) force fluid through the clean membrane, (ii) overcome the added resistance to flow resulting from pore narrowing and constriction, pore plugging and (iii) overcome a serial resistance to flow due to the build-up of a gel/cake through solute deposition on the upstream face of the membrane.

Correspondence to: Georges Belfort, Bioseparations Research Center, Howard P. Isermann Department of Chemical Engineering, Rensselaer Polytechnic Institute, Troy, NY 12180-3590 (USA).
*Present address: CFC Alternatives Center, Korea Institute of Science and Technology, Seoul (Korea).

Keywords: fouling; rotating annular filter; concentration polarization; liquid permeability and separation; rotary vortex filter; cell culture feed

Introduction

Although pressure-driven crossflow membrane filtration is a very attractive option for many industrial applications, the process is not without problems. Foremost of these is the build-up in solution near the membrane (concentration polarization) and deposit on the membrane (fouling) of dissolved and suspended solutes. A concentrated layer of solute in solution near the membrane–solution interface effects membrane performance through its increased viscosity [1,2], increased osmotic back-pressure [3,4], and resistance to convective and diffusive flows [5]. Additionally, the deposition and adsorption of dissolved and suspended solutes and particles on the face and inside the porous structure of a membrane usually result in a decrease in permeation flow rate through pore constriction and plugging and build-up of secondary layers on the membrane [6]. These phenomena also effect membrane selectivity.

To gain a better understanding of these limitations, several direct and indirect approaches have been used. Earlier work focussed on the effects of varying pH and ionic strength of suspensions [7–9] and solutions [10–12] on the permeation flux (called "flux" from now on) and solute retention.

Suspensions. Decreasing the stability of suspensions through salt addition can result in colloidal flocculation with an increase in the mean particle size and a decrease in the flow resistance of the deposited secondary layers on the membrane face [7]. Using pH changes with a colloidal suspension, Cohen and Probstein [8] were able to change the rate of colloidal agglomeration and hence flux. Thus, by aggregating the suspending particles larger flocs rather than individual particles reach the membrane and significantly effect the flux-reducing fouling layer [9].

The hydrodynamic behavior of dilute suspensions in membrane ducts has been studied theoretically [13–18] and experimentally [18–20]. Inertial lift due to the acceleration terms in the Navier–Stokes equations [13–15,19] and shear-induced diffusion resulting from particle motion due to axial drag at the solution–cake interface [16–18,20] have been proposed to augment Brownian diffusion and explain the so-called "flux-paradox" [21] where the flux is found to be much higher than predicted [22]. For additional discussion the reader is referred to references [23,24].

Solutions. Much more work has been reported with solutions than with suspensions especially with macromolecules such as proteins [bovine serum albumin (BSA), ovalbumin, and lactoglobulins], poly(vinyl alcohol), poly (ethylene glycol), dextrans and others. The decline of flux with time or total integrated volume permeated was initially explained as membrane compaction. However, it soon became clear that different rates of flux-decline occurred with different solutions under similar experimental conditions. Several phenomena have been proposed to explain this. They include: (1) protein adsorption: the effect of pH and ionic strength on the stability of solute–solute and solute–membrane interactions [10–12,25–28], (2) reduced driving force: the effects of osmotic pressure due to the build-up of macromolecules at the solution–membrane interface [29–33], (3) increased resistance to flow: The effect of protein deposition and gel formation, and increased viscosity of the fluid [6,34–37]. One of the most studied model protein systems for understanding membrane polarization and fouling has been BSA solutions. For example, fluxes are higher when the pH is away from the p*I* of the protein [10,12, 25,34,38], when little salt is present [34], and when the surface chemistry of the membrane is hydrophilic [38]. Recent work on the swelling behavior of adsorbed proteins (Ribonuclease A) on mica support these observations from a fundamental viewpoint [39]. For additional discussion of various direct methods the reader is referred to reference [40].

In many of the studies referred to above it is often difficult to separate the effects of concentration polarization from membrane fouling. Also, in most crossflow membrane modules, transmembrane pressure is coupled to the axial flow rate and hence the axial position along the flow path. Kozinsky and Lightfoot [1] were the first to recognize this more than 20 years ago by choosing a rotating disc membrane system in which the viscous boundary layer thickness is constant with radial distance. The rotating annular filter is another system in which the transmembrane pressure is decoupled from the axial flow rate. Because of this characteristic, we decided to use such a system to study membrane fouling for two commercially relevant cell culture media, serum free and RPMI-1640 with 10% fetal bovine serum. These media are used to grow hybridoma cells to produce monoclonal antibodies for diagnostic, therapeutic and affinity separation purposes [41].

In order to study membrane fouling in a rotating annular filter with the membrane placed on the rotating inner cylinder, we need to solve the Navier–Stokes equations to obtain transmembrane flux at the inner cylinder (membrane) surface as a function of the transmembrane pressure and rotational angular speed. In addition, we will extend and correct the mathematical approach of Meireles et al. [42] to calculate pore constriction resulting from intrapore adsorption by the major component, BSA in the medium. Failing a detailed understanding of protein deposition on the membrane face and its effect on the flux versus transmembrane pressure, we will, recognizing the Langmurian shape of this relationship, invoke a phenomenological approach to obtain a useful model for describing this system as a function of rotational speed.

Theory for rotating annular filtration

Fluid mechanics

Since G.I. Taylor's classic paper of 1923 [43], the behavior of fluid flow in a cylindrical annulus with the inner cylinder rotating at increasing speeds has been the subject of innumerable papers (see Ref. [44] for a partial listing). None to our knowledge have included the porous wall effect. For the following simplified analysis we will ignore the onset of vortex formation, recognizing that the presence of vortices should not unduly influence the pressure in the annulus at the outside surface of the rotating membrane on the inner cylinder. They should, however, together with centrifugal force depolarize solute build-up at the solution–membrane interface.

We consider the system of Fig. 1 in which fluid flows primarily along the z-axis in a cylindrical annulus. The surface of the inner cylinder comprising the annulus consists of a porous membrane while the opposing outer surface is impermeable. One observes experimentally that there exists an "offset" pressure in the dependence of radial flow through the porous membrane on the applied pressure upon rotation of the inner cylinder. Our goal is then to formulate and solve a model of the fluid flow within the cylindrical annulus in order to examine the dependence of this offset pressure on rotational velocity. We will couple an approximation of the Navier–Stokes equations with a Darcy's law expression of the porous membrane.

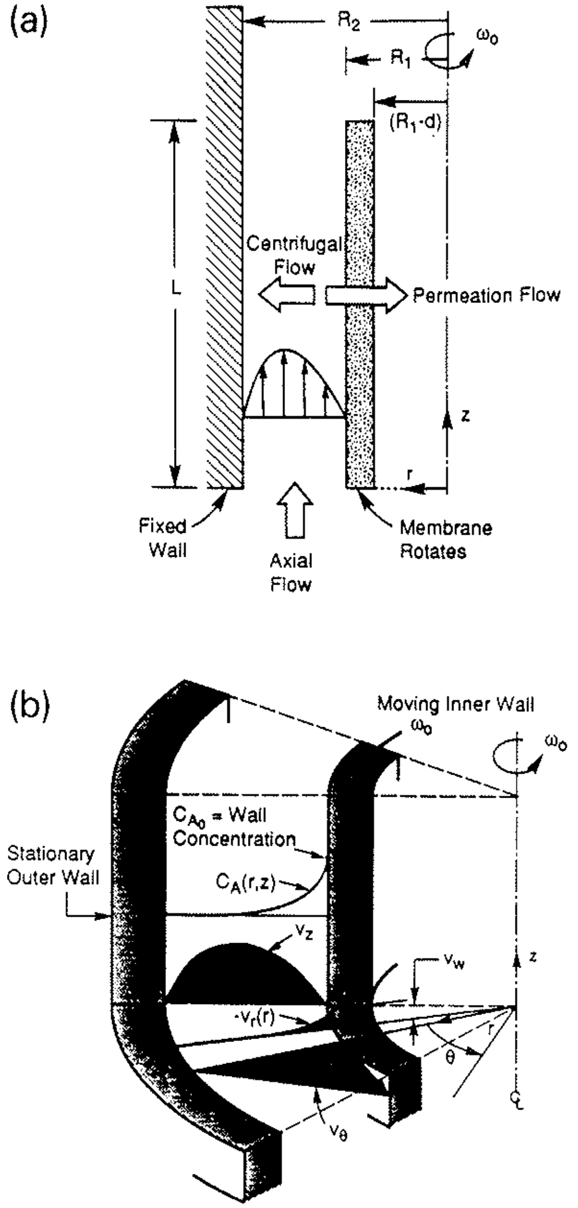

Fig. 1. Coordinate system for flow in an annular rotating filter (a) 2-D coordinates with dimensions, and (b) 3-D coordinates showing the velocity distributions for the v_r, v_θ and v_z components.

In terms of the pressure p, kinematic viscosity ν, density ρ and velocity function $\boldsymbol{v}$, the Navier–Stokes equations describe the fluid flow as

$$\nabla\cdot\boldsymbol{v}=0$$

$$\boldsymbol{v}\cdot\nabla\boldsymbol{v}=-\rho^{-1}\nabla p+\nu\nabla^2\boldsymbol{v}. \tag{1}$$

Expressing the vector differential operators in terms of cylindrical coordinates (r, θ and z), the usual boundary conditions for the velocity component v_θ applies: this tangential velocity vanishes on the outer wall at R_2 and is equal to the rotating wall velocity $\omega_o R_1$ at radius R_1. For the radial velocity v_r, we take this normal component to be zero at the outer (impermeable) wall and proportional to the pressure difference across the porous membrane at the inner wall.

We approximate the flow as having a weakly coupled z-component. Specifically, we take the axial flow to be that arising from a weak, constant pressure gradient when both inner and outer boundaries are impermeable. This idealized flow, which depends only on the radial coordinate, then feeds a small radial flow that describes the flow through the membrane of the inner boundary. In this approximation, there then exists an angle-independent solution to eqn. (1) for the radial and azimuthal components of the flow. Since the three velocity components and the pressure gradient vary only with radius r, the governing equations for v_r, v_θ and pressure p become

$$v_r\frac{\mathrm{d}v_r}{\mathrm{d}r}-r^{-1}v_\theta^2=-\rho^{-1}\frac{\mathrm{d}p}{\mathrm{d}r}+\nu\left(\frac{\mathrm{d}^2v_r}{\mathrm{d}r^2}+r^{-1}\frac{\mathrm{d}v_r}{\mathrm{d}r}-r^{-2}v_r\right) \tag{2a}$$

$$v_r\frac{\mathrm{d}v_\theta}{\mathrm{d}r}+r^{-1}v_rv_\theta=\nu\left(\frac{\mathrm{d}^2v_\theta}{\mathrm{d}r^2}+r^{-1}\frac{\mathrm{d}v_\theta}{\mathrm{d}r}-r^{-2}v_\theta\right) \tag{2b}$$

$$\frac{\mathrm{d}(rv_r)}{\mathrm{d}r}=-\frac{\partial v_z}{\partial z} \tag{2c}$$

As per our narrative discussion above, we replace the partial derivative on the right-hand side of eqn. (2c) by a function proportional to the idealized azial flow

$$v_z(r)=\frac{\Delta p_{tc}}{4\mu L}\times\left(-r^2+\frac{(R_2^2-R_1^2)\log r+R_1^2\log R_2-R_2^2\log R_1}{\log(R_2/R_1)}\right) \tag{3}$$

where "log" denotes the natural algorithm and Δp_{tc} is the axial pressure drop in the flow direction z.

Solution of eqn. (2c) then provides the radial flow with the boundary condition $v_r(R_2)=0$. Equation (2b) then becomes

$$\nu r^2 v_\theta''+r(\nu-rv_r)v_\theta'-(\nu+rv_r)v_\theta=0 \quad \text{with } v_\theta(R_1)=\omega_0 R_1 \text{ and } v_\theta(R_2)=0 \tag{4}$$

Though eqn. (4) is linear in $v_\theta(r)$, its solution is not expressible in terms of elementary functions since $rv_r(r)$ includes a logarithmic dependence on the radial coordinate. Given that our goal is to compute $v_\theta(r)$ and then insert the result into eqn. (2a) and integrate over r to get $p(r)$, it appears reasonable to replace $rv_r(r)$ in eqn. (4) by the mean value

$$\langle rv_r\rangle=\int_{R_1}^{R_2}\mathrm{d}r\, r(rv_r)\Big/\int_{R_1}^{R_2}\mathrm{d}r\, r= \frac{-q}{24\pi R_1}\left(R_2^3-R_1^3-\frac{(R_2-R_1)^2(R_2+R_1)}{\log(R_2/R_1)}\right)^{-1} \times\left(\frac{-8R_1^3(R_2^3-R_1^3)}{R_2^2-R_1^2}+\frac{R_2^4+R_1^3(8R_2-9R_1)}{\log(R_2/R_1)}\right) \tag{5}$$

where q is the fluid flow into the porous membrane expressed as an area per time. To get the total mass of fluid flow per time, one would multiply q by the length of the system and the density of the fluid. Equation (4) now becomes an Euler equation with two solutions that are simple algebraic powers of radius r [45].

We have finally reached the point where we may consider how to compute the pressure difference generated by the membrane rotation. We shall find the pressure drop across the membrane by combining Darcy's law $v=-\kappa\nabla p$ within the membrane with the radial fluid flow q. Taking the inner permeate side centrifugal pressure to be zero, the resulting drop across the membrane is labeled as $p(R_1)$ with

$$p(R_1)=\frac{q}{2\pi\kappa}\log\frac{R_1}{R_1-\bar{d}} \tag{6}$$

As the last step, we integrate eqn. (2a) from R_1 to R_2 to get the total offset pressure $p(R_2)$ and find

$$\begin{aligned}p(R_2)={}&\frac{q}{2\pi\kappa}\log\frac{R_1}{R_1-\bar{d}}\\&+\frac{q\rho\nu}{2\pi R_1^2}\frac{R_2^2-(R_2^2-R_1^2)/\log(R_2/R_1)}{R_2^2+R_1^2+R_1R_2-(R_2^2-R_1^2)/\log(R_2/R_1)}\\&+\frac{\rho q^2}{8\pi^2R_1^2}+\frac{\rho\omega_0^2}{2\Delta^2}\Bigg\{(R_1^{-2}-R_1^{-2})R_2^{2q\beta/2\pi\nu}\\&-\frac{8\pi\nu}{q\beta}R_2^{-2+q\beta/2\pi\nu}(R_2^{q\beta/2\pi\nu}-R_1^{q\beta/2\pi\nu})\\&+R_2^{-4}\left(1+\frac{q\beta}{2\pi\nu}\right)^{-1}(R_2^{2+2q\beta/2\pi\nu}-R_1^{2+2q\beta/2\pi\nu})\Bigg\}\end{aligned} \tag{7}$$

In eqn. (7), we have employed the definitions

$$\Delta\equiv R_1^{-2}R_2^{q\beta/2\pi\nu}-R_2^{-2}R_1^{q\beta/2\pi\nu}$$

and

$$\beta\equiv-2\pi<rv_r>/q.$$

Equation (7) is admittedly quite difficult to interpret. We can simplify the expression enormously by taking the membrane thickness $\bar{d}$ and annular spacing R_2-R_1 to be much less than the radius R_1. The lowest order expansion of eqn. (7) in these two limits becomes

$$p(R_2) \approx \frac{q}{2\pi R_1}\left(\frac{\bar{d}}{\kappa}-\frac{\rho\nu}{R_1}\right)+\frac{\rho q^2}{8\pi^2 R_1^2} + \rho\omega_0^2 R_1^2\left(\frac{R_2-R_1}{3R_1}\right) \tag{8}$$

Since we analyze the experimental data by plotting q as a function of pressure p, we rewrite this expression as

$$q=\frac{2\pi R_1}{\rho}\left(\frac{\bar{d}}{\kappa}-\frac{\rho\nu}{R_1}\right) \left(-1+\sqrt{1+2\rho\left(\frac{\bar{d}}{\kappa}-\frac{\rho\nu}{R_1}\right)^{-2}\left[p-\rho\omega_0^2 R_1^2\left(\frac{R_2-R_1}{3R_1}\right)\right]}\right)$$

$$\approx \frac{2\pi R_1}{\frac{\bar{d}}{\kappa}-\frac{\rho\nu}{R_1}}\left[p-\rho\omega_0^2 R_1^2\left(\frac{R_2-R_2}{3R_1}\right)\right] - \frac{\pi R_1\rho}{\left(\frac{\bar{d}}{\kappa}-\frac{\rho\nu}{R_1}\right)^3}\left[p-\rho\omega_0^2 R_1^2\left(\frac{R_2-R_1}{3R_1}\right)\right]^2 \tag{9}$$

As documented, our derivation included several simplifications. We took the components of the flow to be idealized (essentially laminar) without vortices and weakly coupled. The subsequent quantitative observation that the pressure offset varies as the square of the rotation frequency tends to validate this treatment. If the velocity flow components were more strongly coupled – as one should expect with larger flow rates – then the effect of rotation would be more pronounced and complicated than a simple pressure translation. We also recall that we simplified the azimuthal flow eqn. (4) by replacing $rv_r(r)$ by its mean value $<rv_r>$. This approximation is reasonable since the asymptotic limit of eqn. (8) is completely unaffected. The parameter β, which measures the ratio of $<rv_r>$ to $R_1 v_r(R_1)$ does not appear at lowest order as $(R_2-R_1)/R_1$ approaches zero.

Finally, the wall velocity or flux is given by (with $p=\bar{p}$)

$$v_w = -v_r(R_1) = \frac{q}{2\pi R_1} \approx \frac{\kappa}{\bar{d}}\left(\bar{p}-\rho\omega_0^2 R_1^2\frac{R_2-R_1}{3R_1}\right) \approx a(\bar{p}-b\omega_0^2) \tag{10}$$

The term outside the parenthesis is the permeability coefficient divided by the membrane thickness while the second term in the parenthesis is the pressure off-set term and depends on the square of the rotational speed as expected. A plot of flux v_w versus the actual pressure at the membrane surface $(\bar{p}-b\omega_0^2)$ should give a universal plot independent of rotational speed. A courser but simpler derivation of eqn. (10) suggested by a reviewer is given in Appendix A.

Changes in membrane pore size distribution

Consider a particle of diameter d and a pore of diameter d_p as shown in Fig. 2. For the case when $d \ll d_p$, the particles could enter most pores and could conceivably close smaller pores thereby reducing the open cross-sectional area for flow. This is shown schematically as a loss of pores from the pore size distribution and a decrease in the slope of the flux as shown in Fig. 2. A similar effect occurs when $d \approx d_p$ and some pores are lost because of pore plugging. For the case when $d \gg d_p$, the particles are unable to enter most pores and hence deposit on the face of the membrane resulting in gel/cake build-up. Assuming the pore size distribution of the membrane remains the same as for a clean membrane, the shape of the pore size distribution of the gel/cake will most likely change with time and transmembrane pressure. Compaction, rearrangement and deposition of smaller particles in the pores of the gel/cake (as de-

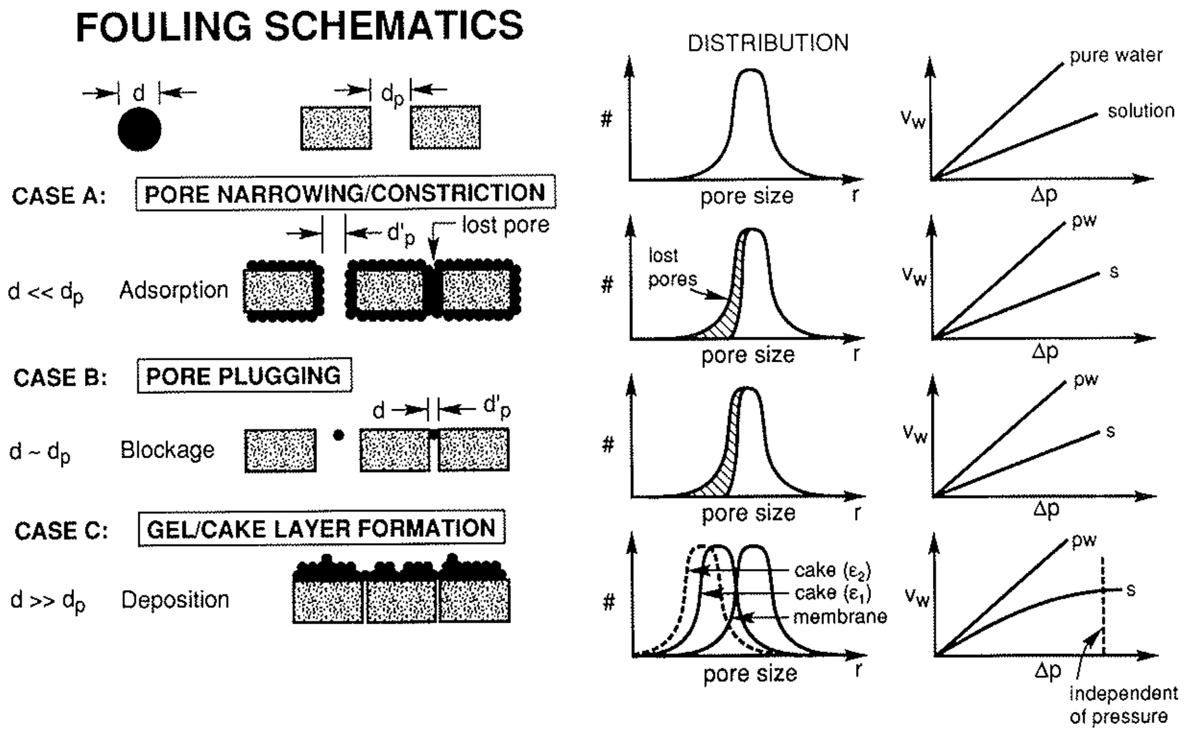

Fig. 2. Fouling schematics: (Case A) pore narrowing and constriction, (Case B) pore plugging, and (Case C) solute deposition and gel and cake layer formation.

scribed for the first case above) could explain this. In this case, the slope of the flux versus transmembrane pressure curve will decrease with increasing pressure (Fig. 2). This is often observed experimentally and has been attributed to increased deposit thickness [6] and/or osmotic effects [32].

Following Meireles et al.'s [42] approach, assuming a corrected log normal pore size distribution, $n(r)$, and assuming that the local flow rate through a pore, $j(r)$, is given by Poiseuille flow, then the solvent flux is given by

$$v_w = \int_0^\infty j(r)n(r)\mathrm{d}r \tag{11}$$

where the number of pores per unit area is

$$n(r) = \frac{n_o}{r\sqrt{2\pi}}\left[\log(1+(\sigma/r^*)^2)\right]^{-1/2} \times \exp\left\{\frac{-\left[\log(r\sqrt{1+(\sigma/r^*)^2})/r^*\right]^2}{2\log(1+(\sigma/r^*)^2)}\right\} \tag{12}$$

and

$$j(r) = \text{velocity} \times \text{area} = (\Delta\bar{p}r^2/8\mu l)\pi r^2 \tag{13}$$

where n_o is the probability density of radius r, r^* is the mean radius, σ is the standard deviation of the distribution, μ is the kinematic viscosity and eqn. (13) is called the Hagen–Poiseuille law. Unfortunately, r^* and σ^2 as used by Meireles et al. [42] in their eqn. (2) are not the mean and variance of their expression, respectively, as evaluated by moment analysis. Equation (12) on the other hand, does give the mean r^* and variance σ^2 by moment analysis correctly.

Substituting eqns. (12) and (13) into eqn. (11) and rearranging gives a modified flux

$$S_1=\frac{v_w}{\left(\frac{n_o}{l}\right)\left(\frac{\pi\Delta\bar{p}}{8\mu}\right)}$$

$$=\{2\pi\log[1+(\sigma/r^*)^2]\}^{-1/2}$$

$$\times\int_o^\infty \exp\left\{\frac{-[\log(r\sqrt{1+(\sigma/r^*)^2}/r^*)]^2}{2\log(1+(\sigma/r^*)^2)}\right\}r^3\mathrm{d}r$$

$$=(r^*)^4[1+(\sigma/r^*)^2]^6 \tag{14}$$

Assuming that $k=it$ is the thickness of an adsorbed multilayer inside a pore and that t is the thickness of an adsorbed monolayer (a dimension that can be estimated from the molecular structure of a protein or macromolecule), then i is the number of monolayers adsorbed in the pore. To account for the loss in cross-sectional area for flow through a pore, r is now substituted for by $r-k$ in eqn. (13). Since the number of pores per unit membrane area remains the same, eqn. (12) is unaltered. Explicit expressions (eqn. 14) for the modified fluxes without and with adsorbed solute in the pores are presented in the Appendix B. Their ratio is

$$S=S_2/S_1=1-\frac{4}{q^3}\left(\frac{k}{r^*}\right)+\frac{6}{q^6}\left(\frac{k}{r^*}\right)^2$$

$$-\frac{4}{q^6}\left(\frac{k}{r^*}\right)^3+\frac{1}{q^5}\left(\frac{k}{r^*}\right)^4 \tag{15}$$

where $q=1+(\sigma/r^*)^2$. Equation (15) can conveniently be used to obtain an estimate of k assuming that σ is the same for the membrane with and without adsorbed solute. The model assumes that on an average the adsorbed layer is uniform throughout. At present little is known on how reasonable this assumption is.

In Fig. 3 the integrand of eqn. (14) with r substituted by $(r-it)$ in the flow component (eqn. 13) is plotted as a function of pore radius r for different numbers of monolayers ($i=0, 10, 20, 30$) with the molecular diameter of $t=72.2$ Å for bovine serum albumin, the geometric standard deviation, $\sigma=0.48$ μm (chosen from Belfort et al., [46]), and the mean radius of the membrane pores, $r^*=0.62$ μm. Substituting σ as a function of r^* and a known value of the mode $r_m=0.305$ μm (from measurements) into $r_m=(r^*)^4/[(r^*)^2+(\sigma)^2]^{3/2}$ and then into eqn. (15), allows one to calculate S as a function of r^* only. Subtracting the measured S values from the calculated values of S and squaring the difference for two cases, we obtained the best-fit r^* and σ values [46]. For the hydrophilic microfiltration membrane, we obtained best-fit values of $r^*=0.62$ μm and $\sigma=0.48$ μm which were used in preparing Figs. 3 and 4. As the number of adsorbed layers increases, both the peak of the modified frequency, f, and the area under the curves decrease as expected. Knowing the slope of the flux–transmembrane pressure curve for clean water ("no fouling" case) and for the case with protein solution from experiments, an estimate of the number of layers

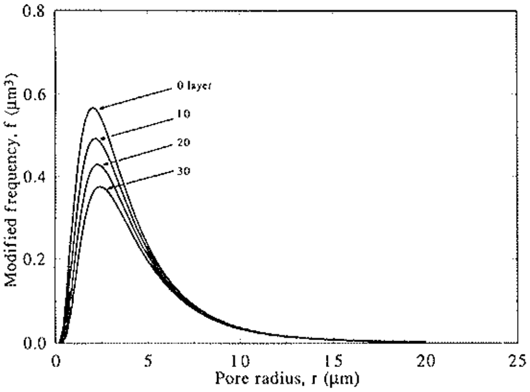

Fig. 3. Plot of the integrand of eqn. (14) (called the modified frequency, f) with r substituted by $(r-it)$ in eqn. (13) versus pore radius, r for different numbers of adsorbed layers i assuming $r^*=0.62$ μm and $\sigma=0.48$ μm and $t=72.2$ Å.

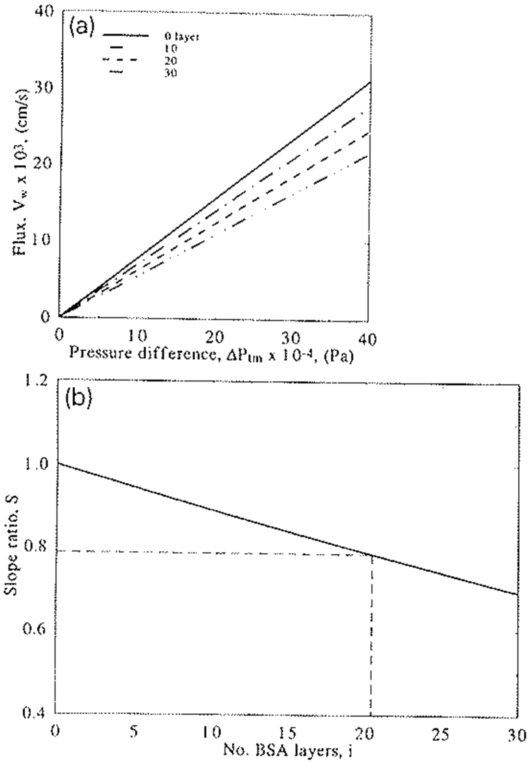

Fig. 4. (a) Flux versus transmembrane pressure difference for different numbers of adsorbed layers i, assuming $r^* = 0.62$ µm and $\sigma = 0.48$ µm and $t = 72.2$ Å for BSA. The initial slope for $i = 0$ is obtained experimentally (choose 0.783E−7 cm/sec-Pa from Fig. 7) and determines n_o/l from eqn. (14). Assuming σ to be the same for the clean ($i = 0$) and the surface covered ($i > 0$) membranes, eqn. (15) is used to determine the decrease in slope resulting from adsorption of one or more monolayers. (b) Slopes from (a) as a function of i for $\sigma = 0.48$ µm according to eqn. (15).

i of protein adsorbed in the pores can be obtained from eqn. (15) knowing r^*, σ and t (Fig. 4).

Gel/cake layer formation

Consider the case where the particle or solute is too large to penetrate the largest pores of the membrane (Case C, Fig. 2), then deposition onto the face of the membrane is expected. The mechanism or physics of this process is barely understood. Some have used particle trajectory analysis to describe the arrival of particles at the surface [19] and others have used simulation with "sticking and orientation rules" to describe cake formation and build-up [47]. Still, these methods are complicated and difficult to generalize. Here, we will use a phenomenological approach by realizing that the typical shape of the flux versus transmembrane pressure curve for membranes with deposited gels/cakes is reminiscent of the shape of the Langmuir adsorption isotherm. Hence from a simple resistance model

$$v_w = \frac{\Delta\bar{p}}{R_m + R_c} \tag{16}$$

where R_m is the membrane resistance to flow, and $R_c = \tilde{b}\Delta\bar{p}$, the pressure-dependent cake resistance; $\Delta\bar{p} = (\bar{p} - b\omega_0^2)$ from eqn. (10), corrected transmembrane pressure difference, where $b\omega_0^2$ is the offset centrifugal pressure obtained from a deionized (DI) water run with the same membrane. Since we do not know the Stavermann reflection coefficient, $\bar{\sigma}$, we have decided to incorporate the usual osmotic term in the numerator ($-\bar{\sigma}\Delta\pi$) into the cake resistance term R_c (or b_o) in the denominator. This simplifies the analysis by reducing the number of parameters by one. We also find it unnecessary to express R_o in terms of $\Delta\bar{p}^n$ where n is some number approximately 0.5 to describe compression of the cake. Inverting eqn. (16)

$$v_w^{-1} = \frac{R_m}{\Delta\bar{p}} + \tilde{b} \tag{17}$$

but the intercept $\tilde{b}$ is dependent on rotational speed

$$\tilde{b} = b_o\omega_o^n \tag{18}$$

Substitute for R_c and $\tilde{b}$ above into eqn. (16), obtains

$$v_w = \frac{\Delta\bar{p}}{R_m + b_o\omega_o^n\Delta\bar{p}} \tag{19}$$

First, the experimental data are plotted according to eqn. (17) to obtain $\tilde{b}$ for each ω_o, then this data are fitted to the power eqn. (18) to obtain b_o and n. The membrane resistance R_m is obtained from the linear slope of flux versus transmembrane pressure for a "clean" (deionized water) run where $R_c=0$. The derived parameters are then used in eqn. (19) for predicting flux from transmembrane pressure.

Experimental

Materials

Three different feed solutions including two commercially relevant cell culture media and deionized water as a control were used in this study. Details of their preparation were as follows: (1) deionized water (designated DI water) prepared by passing Troy tap water through ion exchange, activated carbon adsorption, reverse osmosis (with FT-30 composite polyamide membrane, FilmTech Corp., MN), and UV. The conductivity of the water was about 19 megohm (i.e. $\pi=0$), (2) a commercial basal nutrient serum-free medium (designated SF medium and obtained from W.R. Grace and Co. MA as WRC 935) comprising of essential and non-essential amino acids and amino acid derivatives, bulk ions and trace elements, buffers, vitamins, coenzymes, carbohydrates and derivatives, nucleic acid derivatives, and lipids according to the formulation described in a recent European Patent Application [48] and publication [49]. The total osmolarity of the basal medium was $\pi=300$ mosm, (3) A commercial whole medium (designated 10% FBS) containing 10% fetal bovine serum (FBS, the major component of which is bovine serum albumin, BSA) and RPMI 1640 medium [50], which contains inorganic salts, hepes, carbohydrates, amino acids and derivatives, vitamins and antibiotics. The total osmolarity of this medium is approximately $\pi=282$ mosm.

Rotating system

A commercial laboratory rotating filter with the membrane placed on the inner rotating cylinder (Benchmark, Membrex, Inc., Fairfield, NJ) was used as shown in the flow sheet in Fig. 5. Permeate and recycled retentate were returned continually to the reservoir. Design and operating details of the rotating filter are summarized in Table 1. Wall shear at the membrane surface is mainly dependent on angular rotation and hence Taylor number $[Ta=[(R_1\omega_o(R_2-R_1)/\nu](R_2-R_1/R_1)^{0.5}]$

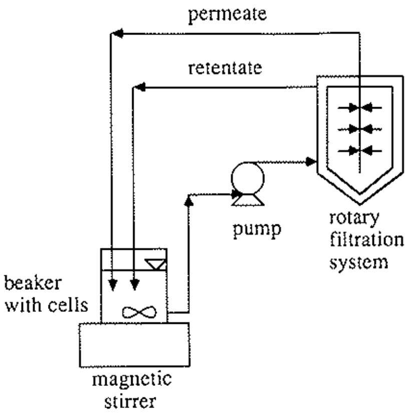

Fig. 5. Rotary filtration system.

TABLE 1

Design and operating details of the rotating membrane system

Inner cylinder	2.205 cm
Annular gap	0.243 cm
Membrane cartridge length	17.0 cm
Effective membrane surface area	200 cm^2
Operational pressure range	0-275 kPa 0-40 psi
Rotational speed range	500-2000 rpm
Taylor number range[a]	931-7452
Axial flow rate	9.75 ml/sec
Axial Reynolds number[b]	183

[a] Taylor number $Ta=[R_1\omega_o(R_2-R_1)/\nu][(R_2-R_1)/R_1]^{0.5}$.
[b] Reynolds number $Re=2v_z(R_2-R_1)/\nu$.

and is essentially decoupled from axial flow or axial Reynolds number $[Re=2v_z(R_2-R_1)/\nu]$. This explains the need for operating at a very low axial Reynolds number. The ratio of the gap width to inner radius $(R_2-R_1)/R_1=0.1102$. For $41.3<Ta<800$, laminar flow with vortices occurs in this system, for $800<Ta<2000$, transitional vortex flow occurs and for $2000<Ta<10{,}000$–$15{,}000$ turbulent flow with vortices dominates the flow. Thus, all of the runs were conducted in the transitional and turbulent vortex regimes.

The actual pressure inside the rotating annulus was measured using a pressure gauge after the exit port of the retentate stream and adding a correction of 18.56 kPa (2.7 psi). This shift in the pressure was confirmed by a series of calibration tests (not shown). For each feed solution, membrane and rotational speed, the flux (volumetric permeate flow rate divided by 200 cm^2) and transmembrane pressure were noted. Then the rotating filter was set to another (usually higher) rotational speed and the flux–transmembrane pressure data were noted. In all 500, 1000, 2000, 3000, and 4000 rpm were used for each feed and membrane at five different transmembrane pressures. The order of measurement was from high to low pressures. Also, since the permeate was open to atmosphere, its pressure was assumed to be 101.1 kPa (14.7 psi). A small error may result from this assumption since the permeate is also exposed to centrifugal force and the pressure maybe somewhat greater than atmospheric.

Membranes

Two different membranes were used in this research. They included: a nominal mean pore size of 0.45 μm hydrophilized (sulfonated) polysulfone microfiltration membrane and a 100 kDa molecular weight cut-off (MWCO) polyacrilonitrile ultrafiltration membrane. According to Membrex Inc., the actual mode pore diameter for the microfiltration membrane was approximately 0.305 μm (D.P. Yavorsky, private communication). Both membrane types were obtained from Membrex Inc., Fairfield, NJ, attached to a cylindrical cartridge. The thicknesses, $\bar{d}$, of these membranes are all about 0.025 ± 0.001 cm. Thus $\bar{d}/R_1=0.0113$.

Results and discussion

Microfiltration membrane (0.45 μm)

Flux versus transmembrane pressure data for five rotational speeds were obtained for the three feed solutions – DI water, SF medium and 10% FBS. An example showing how these measurements were plotted and how the transmembrane pressure was corrected by subtracting the off-set pressure as suggested by eqn. (10) is presented for the SF medium in Fig. 6. A plot of the raw data is shown in Fig. 6(a). From each set of data at a particular rotational speed ω_o, the off-set pressure was obtained from the intercept on the horizontal axis (relative to the 500 rpm run). To check the expected square dependence on ω_o the off-set pressure was plotted against ω_o^2 in Fig. 6(b). Notice the excellent linear correlation $(R^2=0.9999)$. Next, the off-set pressure associated with each rotational speed is subtracted from the measured pressure in order to obtain the actual pressure responsible for driving the permeate through the membrane. This corrected transmembrane pressure was then used to plot all the flux data in Fig. 6(c). All the data collapses onto one universal curve as expected from eqn. (10) with a linear correlation coefficient of $R^2=0.9485$! A similar approach was used for the DI and the 10% FBS medium. The final universal plots for all three feeds are shown in Fig. 7 together with their slopes. Note that the DI water shows the steepest slope (7.83E – 7 cm/sec-Pa), followed by the slope for the SF medium (7.53E – 7) and

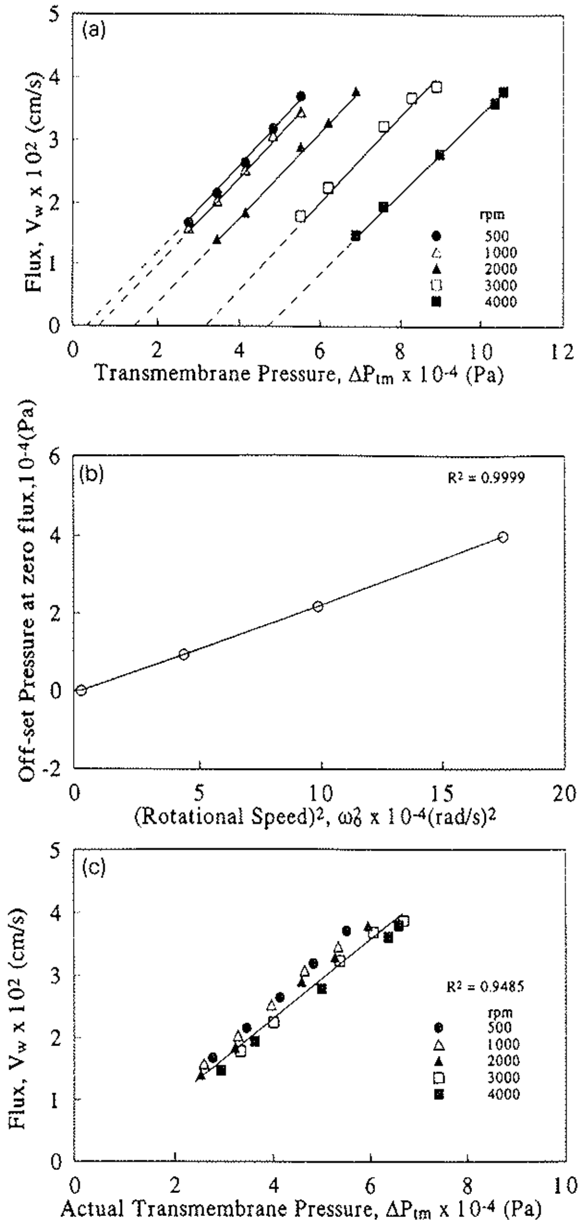

Fig. 6. Microfiltration of a serum-free medium with a nominal 0.45 μm pore size polysulfone membrane. (a) Flux versus measured transmembrane pressure at different rotational speeds. The off-set or centrifugal pressure for each rotational speed relative to the 500 rpm run is obtained by extending the linear plots to the horizontal axis. (b) Off-set pressure at zero flux versus square of the rotational speed. (c) Flux versus modified or actual transmembrane pressure for all the runs from (a). The data collapse onto one linear line. This is a test for eqn. (10).

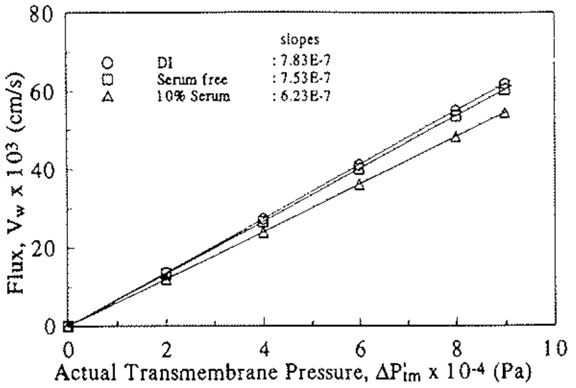

Fig. 7. Universal flux versus actual transmembrane pressure for deionized water (DI), serum-free medium (SF) and 10% fetal bovine serum (10% FBS) with a nominal 0.45 μm mean pore size polysulphone microfiltration membrane.

by the slope for the 10% FBS medium (6.23E−7). The slope ratios relative to the DI water were 0.962 and 0.796 for the SF medium and the 10% FBS medium, respectively. For the 10% FBS medium, from eqn. (15) or Fig. 4(b) this gives 21 layers of BSA lining the pores of the nominal 0.45 μm microfiltration membrane, with log-normally distributed pore sizes ($r^*=0.62$ μm, $r_m=0.305$ μm and $\sigma=0.48$ μm). This predicts a 42% loss in the cross-sectional area for flow in the mean pore of radius r^*. For smaller and larger pores this percent loss increases and decreases respectively as shown for $i=10$, 20 and 30 in Fig. 3. The net result is a noticeable loss in permeation flux as shown in Fig. 7. This result is somewhat surprising as one would not *a priori* expect adsorption of proteins into the pores of a microfiltration membrane to be that effective in reducing the permeation flux.

Note that there is a discrepancy between the predicted value (0.31×10^4 Pa) and the measured value (4.6×10^4 Pa in Fig. 6a) for the off-set pressure at 4000 rpm. A likely reason to explain this is the effect of neglecting the permeate centrifugal pressure [estimated at 4.2×10^4 Pa in Appendix C]. Also, since the data is corre-

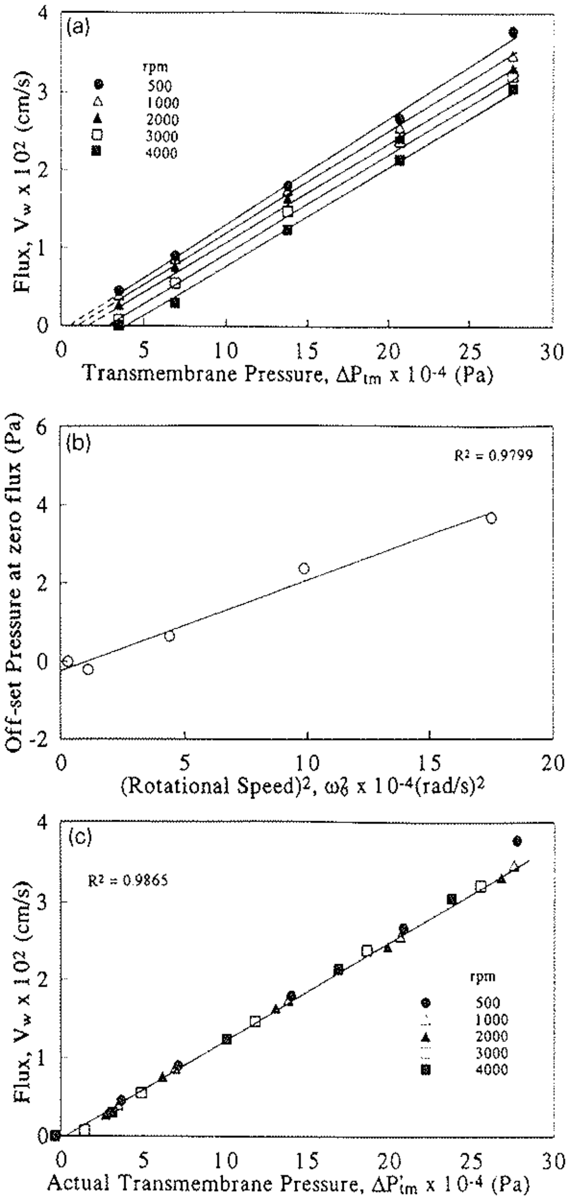

Fig. 8. Ultrafiltration of deionized water (DI) with a 100 kDa MWCO polyacilonitrile membrane. (a) Flux versus measured transmembrane pressure at different rotational speeds. The off-set or centrifugal pressure for each rotational speed relative to the 500 rpm run is obtained by extending the linear plots to the horizontal axis. (b) Off-set pressure at zero flux versus square of the rotational speed. (c) Flux versus modified or actual transmembrane pressure for all the runs from (a). The data collapse onto one linear line. This is a test for eqn. (10).

lated to the 500 rpm case, it is not expected to pass through the origin in Fig. 6(a).

The discussion above focuses mainly on pore narrowing and constriction and pore plugging as described qualitatively in Fig. 2 in Cases A and B. This is appropriate for the adsorption of small proteins such as BSA onto the internal pore surface of a large pore microfiltration membrane. Note that these effects cause a change in the constant slope but not in the linearity of the flux–pressure curves. Next, we will address Case C, gel/cake build-up or deposition onto the outer (upstream) face of a small pore ultrafiltration membrane. Here the slope of the flux–pressure curves decreases with increasing transmembrane pressure.

Ultrafiltration membrane (100 kDa MWCO)

Flux versus transmembrane pressure data for five rotational speeds were obtained for the three feed solutions – DI water, SF medium and 10% FBS. The results for the DI water are shown in Fig. 8, where it can be seen that, as with DI water and the nominal 0.45 μm microfiltration membrane, the flux–pressure plots are linear (Fig. 8a) and decrease in amplitude with increasing rotational speed. This emphasizes that without fouling centrifugal force diminishes the transmembrane pressure and hence the flux (eqn. 10). The off-set pressure correlates well with the square of the rotational speed (Fig. 8b, $R^2=0.9799$) and when used in a universal plot of flux versus actual transmembrane pressure (measured transmembrane pressure minus centrifugal pressure) one obtains an excellent fit for all the data (Fig. 8c, slope=1.25E−7 cm/sec-Pa, $R^2=0.9865$). This confirms the form of eqn. (10). Note that the slope for this UF membrane is 16% of that measured for the MF membrane for DI water.

The results for the 10% FBS medium are shown in Fig. 9. The profiles of these curves are completely different to those for the DI water.

The most significant differences are that the amplitude of the flux is increased with increasing rotational speed and that the curves are convex in shape with "Langmuir-like" behavior. The former highlights the advantage of using the rotational filter and the latter suggests a pressure-dependent gel/cake resistance in eqn. (16). Note in Fig. 9(a) for one measurement point ($\Delta P_{\mathrm{tm}}=104$ kPa) the flux for the 4000 rpm run falls below that for the 3000 rpm run. Using the off-set values for each rotational speed from Fig. 8(a) and (b), flux is plotted against actual transmembrane pressure in Fig. 9(b). Due to the increasing horizontal negative shift with rotational speed (look at the highest pressure points), flux is always highest for any given pressure at the largest rotational speed. Also note that an imaginary linear line can be drawn through the lowest pressure points for the top three rotation speeds (slope = 0.714E−7 cm/sec-Pa). The low pressure data appear to converge to this line. From the data and analysis for the nominal 0.45 μm microfiltration, this imaginary line is most likely the result of pore narrowing and constriction, pore

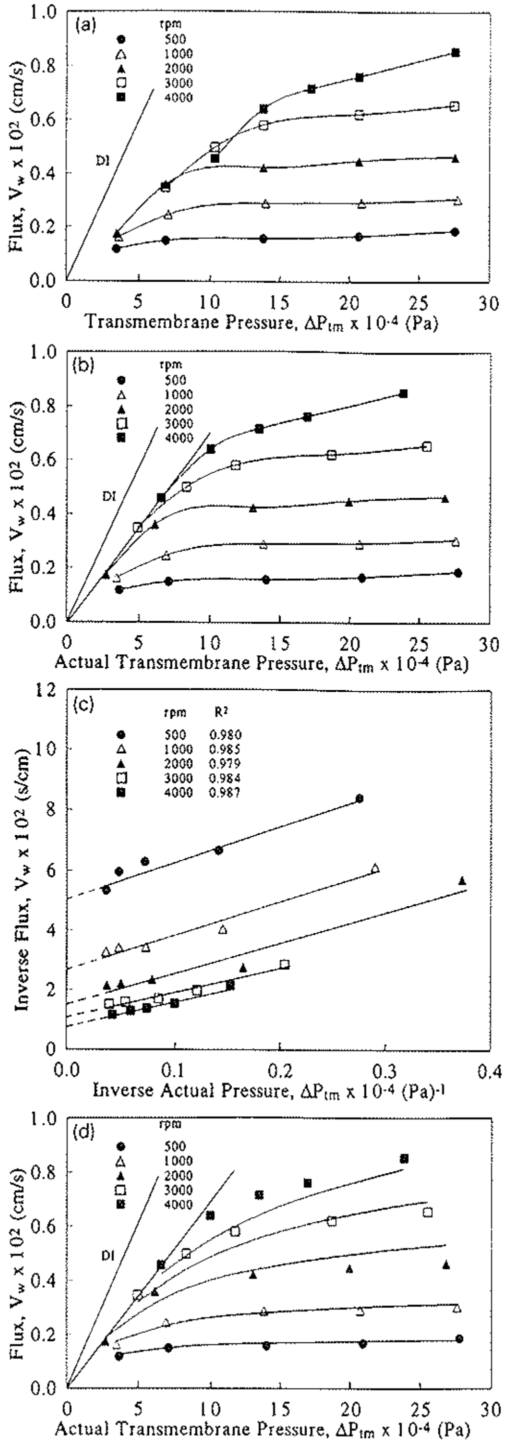

Fig. 9. Ultrafiltration of 10% fetal bovine serum with a 100 kDa MWCO polyacilonitrile membrane. (a) Flux versus measured transmembrane pressure at different rotational speeds. The line for deionized water (DI) is taken from the linear correlation in Fig. 8(c). The lines through the data are four coefficient polynomials. (b) Flux versus actual transmembrane pressure for all the runs from (a). The actual transmembrane pressures were obtained by subtracting the off-set pressures for DI water from Fig. 8(b) from the measured pressure. The lines through the data are four coefficient polynomials. The second and lower slope line is the imaginary line through the lowest pressure data points for the highest three rotational speeds. (c) The data in (b) are replotted as an inverse plot according to eqn. (17). Linear correlations of each set of data at different rotational speeds obtaines R_{m} (mean of the slopes) and $\tilde{b}(\omega_{\mathrm{o}})$ (vertical intercept). A correlation between $\tilde{b}$ and ω_{o} (not shown) gives the two coefficients b_{o} and n (see text). (d) The two linear lines and data are replotted and compared with predictions by eqn. (19) using the coefficients obtained from (c) above.

plugging and osmotic effects [51,52] as described qualitatively in Fig. 2 in Cases A and B. The ratio of the flux–pressure slopes for a BSA solution as compared to DI water for a 100 kDa MWCO UF membrane was 0.571 for this study and 0.575 for another study [40]. For the latter study, DI water was passed through a clean membrane and a membrane preadsorbed with BSA.

For attaining a given flux (choose any flux in Fig. 9(b) and move horizontally along this line parallel to the pressure coordinate), the pressure between the two linear lines, i.e. the line for DI water and the imaginary line for pore narrowing and constriction, pore plugging and osmotic effects, is the added pressure needed to overcome these phenomena. Additionally, the pressure between the imaginary line for pore narrowing and constriction, pore plugging and osmotic effects and the line through the data points is the added pressure across the gel/cake layer [51,52]. As is well known experimentally, at some point any increase in pressure has a marginal effect on the flux, this has been termed the "pressure-independent" region. The lines through the data in Figs. 9(a) and (b) are polynomial lines (four coefficients) and not based on a model. To test the usefulness (not validity since the model is phenomenological) the data from Fig. 9(b) are plotted according to eqn. (17) as an inverse plot in Fig. 9(c). Linear correlations through each velocity set are all above 0.979 confirming the usefulness of the approach. The slopes of these lines is the membrane resistance, R_m ($=10.11\text{E}+7 \pm 1.44\text{E}+7$ Pa-sec/cm) and the intercepts with the vertical axis gives $\tilde{b}(\omega_o)$. Relating each $\tilde{b}$ (in units of sec/cm) to ω_o through the power relation, eqn. (18), obtains $b_o = 1.847\text{E}+4$ and $n = -0.900$. With these three parameters, eqn. (19) is compared with the data from Fig. 9(b) for each rotational speed and shown in Fig. 9(d). The model appears to be fairly good at predicting the fluxes especially at low and intermediate rotational speeds. At high rotational speeds, the model predicts the correct trend but underpredicts the amplitude of the fluxes.

Although we have focussed our attention in this paper on using a rotating filter as a device to study membrane fouling, it should also be recognized that filter modules similar to the one we have used are being evaluated for many different separations [53]. Lopez-Leiva was perhaps the first to suggest the use of Taylor vortices to depolarize solute build-up at the membrane–solution interface [54]. He also showed its efficacy by building a crude membrane module. About the same time, Lieberherr [55] built a sofisticated rotating filter and tested various kaolinite solutions, proving that the Taylor vortices could indeed reduce cake build-up on the rotating inner porous cylinder. Sulzer AG, Winterthur, Switzerland then commercialized their BDF or "Biodruk" rotating filters [56] and after this Membrex Inc., Garfield, NJ followed suite. Kroner and coworkers have conducted a series of experiments probing the range of applications for the BDF rotating filters [57,58]. Others have recently reported on phenomenological mass transfer correlations for both ultrafiltration and microfiltration in a rotating filter [59,60].

Summary and conclusions

Summary

In an attempt to better understand the different aspects of membrane fouling, we have used a rotating annular filter in which the transmembrane pressure is decoupled from the axial flow rate. By solving the Navier–Stokes equations with several reasonable simplifications for the flow field in an annulus with a rotating inner porous wall, we have obtained a useful expression for the permeation flow rate (flux) as a function of the actual transmembrane pressure. The actual transmembrane pressure is comprised of the measured annulus pressure minus the centrifugal pressure minus the permeate side pressure. Also, a universal correlation between flux and actual transmembrane pressure is predicted by the theory for any rotational speed.

In addition, we have dissected membrane fouling into pore narrowing and constriction, pore plugging and deposition of a gel/cake onto the upstream face of the membrane. Any reduction in the cross-sectional area for convective flow within the membrane itself, such as adsorption of macromolecules onto the pore surfaces or the plugging of pores by colloidal particles, will result in a drop in flux. This effect is manifest by a drop in the slope of the linear relation of the flux-pressure plot. We model these effects with the help of the approach of Meireles et al. [42] and correct and extend their formalism with explicit solutions. One such explicit solution for the ratio of the flux-pressure slopes (eqn. 15) is particularly useful for estimating the number of adsorbed monolayers of a molecule of known dimensions given a reasonable estimate of the mean radius r^* and the geometric standard derivation σ. These values ($\sigma=0.48$ μm and $r^*=0.62$ μm) were obtained from two independent measurements with different particle size suspensions [46]. Without a detailed understanding of solute deposition on the membrane upstream face and its effect on the flux versus transmembrane pressure, we invoke a phenomenological approach to obtain a useful model for describing this phenomenon as a function of rotational speed. This approach assumes that the resistance to flow through the gel/cake is dependent on transmembrane pressure (through compressibility for example) and inversely dependent on rotational speed (through a balance between convective drag to the membrane and inertial lift, shear-induced diffusion and centrifugal force away from the membrane). In summary, transmembrane pressure is used to (i) force fluid through the clean membrane, (ii) overcome the added resistance to flow resulting from pore narrowing and constriction, pore plugging and (iii) overcome a serial resistance to flow due to the build-up of a gel/cake through solute deposition on the upstream face of the membrane.

Conclusions

To test these theoretical and phenomenological approaches, we have chosen two commercial cell culture media commonly used for producing monoclonal antibodies from hybridoma cells and deionized water as feed solutions. Also, microfiltration and ultrafiltration membranes were chosen. Each experiment was conducted at 5 rotational speeds. The main conclusions from this comparison are:

(1) For solutions containing solutes that are relatively small compared to the mean pore size of the membrane, such as with BSA (Stokes radius 36.1 Å) and nominal 0.45 μm microfiltration membrane, pore narrowing, constriction and plugging are the dominant forms of fouling. This presupposes that the solute will interact with the walls of the membrane pores. Conditions favouring such interaction are (i) a solute that is in a theta (θ) or poor solvent and (ii) a highly energetic (i.e. electrostatic interaction) or denaturing surface such as a hydrophobic material (i.e. polysulfone) and an easily denaturing protein such as BSA. This type of fouling manifests itself in the flux-pressure diagram as a decrease in the slope of a linear plot (Fig. 7).

(2) For solutions containing solutes or their aggregates that are approximately the same size as the mean pore size of the membrane, such as with BSA (Stokes radius 36.1 Å) and 100 kDa MWCO ultrafiltration membrane (about 100 Å mean pore radius) pore narrowing, constriction and plugging and surface deposition onto

the upstream face of the membrane are the main mechanisms of fouling. This type of fouling manifests itself in the flux–pressure diagram as a continuously decreasing slope or convex "Langmuir-like" profile with the lower pressure flux data collapsing to an imaginary linear line of slope less than the DI water flux line (Fig. 9d).

Acknowledgements

Dr. Jim Hilderbrandt previously of Membrex Inc., Fairfield, NJ and Dr. Phil Rolchigo, Membrex Inc., Fairfield, NJ, are gratefully acknowledged for supporting this project with research funds and supplying the rotating filter equipment including membranes and support. We thank Dr. Aaron Heifetz and Dr. Linda Custer, W.R. Grace & Co., Columbia, MD, for supplying the WRC 935 basal nutient serum-free medium and details of its composition. Katherine L. McKinney is also thanked for helping prepare the 10% FBS whole medium. We also acknowledge the valuable comments and suggestions of the reviewers, especially for the simple derivation shown in Appendix A.

List of symbols

a	reduced membrane permeability, $(=\kappa/\bar{d})$ (m^2-sec/kg)
b	constant in eqn. (1), $[=\rho R_1^2(R_2-R_1)/3R_1]$ (Pa)
$\tilde{b}$	constant in eqn. (17), $[R_c/\Delta\bar{p}]$ (sec/m)
$\bar{d}$	membrane thickness (m)
d	annular gap width (m)
d_p	diameter of particle (m)
i	number of layers adsorbed in the pore (–)
j	flux through a pore (m^3/sec)
n_o	number of pores of the average radius per area unit (pores/m^2)
$n(r)$	number of pores per unit area (pores/m^2)
p_F	pressure induced by centrifugal force $(=\rho R_1^2\omega_0^2/2)$ (Pa)
$\bar{p}$	pressure at R_1 (Pa)
p	pressure (Pa)
Δp_{tc}	axial pressure drop (Pa)
Δp_{tm}	transmembrane pressure (Pa)
$\Delta p'_{tm}$	actual transmembrane pressure (Pa)
p_m	membrane permeability (m^2-sec/kg)
r	pore radius (m)
r^*	average radius of the pore size distribution (m)
r_m	mode of the pore size distribution (m)
R_c	resistance of cake layer (m^{-1})
R_m	resistance of membrane (m^{-1})
R_1	outer radius of inner cylinder (m)
R_2	inner radius of outer cylinder (m)
Re	axial Reynolds number (–)
S	modified flux ratio for without and with adsorbed solute in the pore (–)
$S_{1,2}$	pure water, solution slope of V_w vs. Δp_{tm} (m/sec-Pa)
t	thickness of an adsorbed monolayer (m)
Ta	Taylor number (–)
Ta_{cr}	critical Taylor number (–)
v	velocity function (m/sec)
v_w	wall flux (m/sec)

Greek symbols

κ	membrane permeability (m^3-sec/kg)
ν	kinematic viscosity (m^2/sec)
μ	pure fluid viscosity (Pas)
ω_o	angular speed (rad/sec)
ρ	density of fluid (kg/m^3)
ρ_o	density of particles (kg/m^3)
$\bar{\sigma}$	Staverman reflection coefficient (–)
σ	geometric standard deviation of the log-normal pore size distribution (–)

References

1 A.A. Kozinsky and E.N. Lightfoot, Protein ultrafiltration: A general example of boundary layer filtration, AIChE J., 18(5) (1972) 1030.

2 W.N. Gill, D.E. Wiley, C.J.D. Fell and A.G. Fane, Effect of viscosity on concentration polarization in ultrafiltration, AIChE J., 134(9) (1988) 1563.

3 R.L. Goldsmith, Macromolecular ultrafiltration with microporous membranes, Ind. Eng. Chem. Fundam., 10 (1971) 113.

4 P. Aimer and V. Sanchez, A novel approach to transfer limiting phenomena during ultrafiltration of macromolecules, Ind. Eng. Chem. Fundam., 25(4) (1986) 789.

5 W.S. Opong and A.L. Zydney, Diffusive and convective protein transport through asymmetric membranes, AIChE J., 37(10) (1991) 1497.

6 W.F. Blatt, A. Dravid, A.S. Michaels and L. Nelson, Industrial biological waste treatment processes, in: J.E. Flinn (Ed.), Membrane Science and Technology, Plenum Press, New York, NY, 1970, pp. 47.

7 G. Belfort and B. Marx, Artificial particulate fouling of hyperfiltration membranes. II. Analysis and protection from fouling, Desalination, 28 (1979) 13.

8 R.D. Cohen and R.F. Probstein, Colloidal fouling of reverse osmosis membranes, J. Colloid Interface Sci., 114 (1987) 194.

9 R.D. Cohen, Investigation of the effect of solution destabilization on flux enhancement in filtration, J. Membrane Sci., 32 (1987) 93.

10 A.G. Fane, C.J. Fell and A. Suzuki, The effect of pH and ionic environment on the ultrafiltration of protein solutes with retentive membranes, J. Membrane Sci., 16 (1983) 195.

11 E. Mattiasson, The role of macromolecular adsorption in fouling of ultrafiltration membranes, J. Membrane Sci., 16 (1983) 23.

12 M. Nystrom, M. Laatikainen, M. Turku and P. Jarvinen, Resistance to fouling - accomplishments by modification of ultrafiltration membranes, Prog. Coll. Polym. Sci., 82 (1991).

13 F.W. Altena and G. Belfort, Lateral migration of spherical particles in porous flow channels: Application to membrane filtration, Chem. Eng. Sci., 39 (1984) 343-355.

14 F.W. Altena, R.J. Weigand and G. Belfort, Lateral migration of spherical particles in laminar porous tube flows: Application to membrane filtration, Phys. Chem. Hydrodyn., 6(4) (1985) 393.

15 D.A. Drew, J.A. Schonberg and G. Belfort, Lateral inertial migration of a small sphere in fast laminar flow through a membrane duct, Chem. Eng. Sci., 46 (1991) 3219-3224.

16 R.H. Davis and D.T. Leighton, Shear-induced transport of a particle layer along a porous wall, Chem. Eng. Sci., 42(2) (1987) 275-281.

17 G.E. Ogden and R.H. Davis, Experimental determination of the permeability and relative viscosity for fine latexes and yeast suspensions, Chem. Eng. Commun., 91 (1990) 11-28.

18 A.L. Zydney and C.K. Colton, A concentration polarization model for the filtrate flux in cross-flow microfiltration of particulate suspensions, Chem. Eng. Commun., 47 (1986) 1-21.

19 J.R. Otis, F.W. Altena, J.J. Mahar and G. Belfort, Measurements of single spherical particle trajectories with lateral migration in a slit with one porous wall under laminar flow conditions, Exp. in Fluids, 4 (1986) 1-10.

20 C.A. Romero and R.H. Davis, Experimental verification of the shear-induced hydrodynamic diffusion model of crossflow microfiltration, J. Membrane Sci., 62 (1991) 249-273.

21 G. Green and G. Belfort, Fouling of ultrafiltration membranes: Lateral migration and the particle trajectory model, Desalination, 35 (1980) 129-147.

22 M.C. Porter, Concentration polarization with membrane ultrafiltration, Ind. Eng. Chem., Prod. Res. Dev., 11 (1972) 234-248.

23 N. Nagata, K.J. Herouvis, D.M. Dziewulski and G. Belfort, Crossflow membrane microfiltration of a bacterial fermentation broth, Biotechnol. Bioeng., 34 (1989) 447.

24 R.H. Davis, Theory for crossflow microfiltration, in: W.S. Ho and K.K. Sirkar (Eds.), Membrane Handbook, Van Nostrand Reinhold, New York, NY, 1992, p. 1.

25 R.M. McDonogh, H. Bauser, N. Stroh and H. Chmiel, Concentration polarization and adsorption effect in crossflow ultrafiltration of protein, Desalination, 79 (1990) 217-231.

26 B.C. Robertson and A.L. Zydney, Protein adsorption in asymmetric ultrafiltration membranes with highly constricted pores, J. Colloid Interface Sci., 134(2) (1990) 563-575.

27 M. Meireles, P. Aimar and V. Sanchez, Albumin denaturation during ultrafiltration: Effects of operating conditions and consequences on membrane fouling, Biotechnol. Bioeng., 38 (1991) 528-534.

28 H. Nabetani, M. Nakajima, A. Wanatabe, S. Nokao and S. Kimura, Effects of osmotic pressure and adsorption on ultrafiltration of ovalbumin, AIChE J., 36(6) (1990) 907-915.

29 R.L. Goldsmith, Macromolecular ultrafiltration with microporous membranes, Ind. Eng. Chem. Fundam., 10 (1971) 113.

30 W.F. Leung and R.F. Probstein, Low polarization in laminar ultrafiltration of macromolecular solutions, Ind. Eng. Chem. Fundam., 18(3) (1979) 274-278.

31 V.L. Vilker, C.K. Colton and K. Smith, The osmotic pressure of concentrated protein solutions: Effects of concentration and pH in saline solutions of bovine serum albumin, J. Colloid Interface Sci., 79(2) (1981) 548-566.

32 G. Jonsson, Boundary layer phenomena during ultrafiltration of dextran and whey protein solutions, Desalination, 51 (1984) 61-78.

33 J.G. Wijmans, S. Nakao and C.A.. Smolders, Flux limitation in ultrafiltration: Osmotic pressure model and gel layer model, J. Membrane Sci., 20 (1984) 115-124.

34 A.G. Fane, C.J.D. Fell and A.G. Waters, Ultrafiltration of protein solutions through partially permeable membranes. The effect of adsorption and solution environment, J. Membrane Sci., 16 (1983) 211-224.

35 S. Nakao, T. Nomura and S. Kimura, Characteristics of macromolecular gel layer formed on ultrafiltration tubular membrane, AIChE J., 25 (1979) 615-622.

36 S. Nakao and S. Kimura, Analysis of solute rejection in ultrafiltration, J. Chem. Eng. Japan, 14(1) (1981) 32-39.

37 N.P. Tirmizi, Study of UF of macromolecular solutions, PhD Thesis, Department of Chemical Engineering, Rensselaer Polytechnic Institute, Troy, NY, 1990.

38 J.H. Hanemaaijer, T. Robbertsen, Th. van den Boomgaard, C. Olieman, P. Both and D.G. Schmidt, Characterization of clean and fouled ultrafiltration membranes, Desalination, 68 (1988) 93-108.

39 G. Belfort and C.-S. Lee, Attractive and repulsive interactions between and within adsorbed ribonuclease A layers, Proc. Natl. Acad. Sci., 88 (1991) 9146-9150.

40 W.S. Opong and A.L. Zydney, Hydraulic permeability of protein layers deposited during ultrafiltration, J. Colloid Interface Sci., 142(1) (1991) 41.

41 K.L. McKinney, R. Dilwith and G. Belfort, Manipulation of heterogeneous hybridoma cultures for overproduction of monoclonal antibodies, Biotechnol. Prog., 7 (1991) 445.

42 M. Meireles, P. Aimar and V. Sanchez, Effect of protein fouling on the apparent pore size distribution of sieving membranes, J. Membrane Sci., 56 (1991) 13.

43 G.I. Taylor, Stability of a viscous liquid contained between two rotating cylinders, Phil. Trans. Roy. Soc., A 223 (1923) 289.

44 P.G. Drazin and W.H. Reid, Hydrodynamic Stability, Cambridge University Press, Cambridge, 1981.

45 W.E. Boyce and R.C. DiPrima, Elementary Differential Equations and Boundary Value Problems, John Wiley & Sons, New York, NY, 1986.

46 G. Belfort, P. Mikulasek, J.M. Pimbley and K.Y. Chung, Diagnosis of membrane fouling using a rotating annular filter. 2. Dilute particle suspensions of known particle size, J. Membrane Sci., 77 (1993) 23.

47 D. Houi and R. Lenormand, Particle accumulation at the surface of filter, Filtr. Sep., July/August (1986) 238-241.

48 Eur. Patent Application #0 283 924, filing date March 18, 1988.

49 R. Wolf, J.A. Bratz and A.H. Heifitz, A new serum-free medium for monoclonal antibody production, Biotechniques, 6 (1988) 62.

50 G.E. Moore, R.E. Gerner and H.A. Franklin, Culture of normal human leukocytes, J. Am. Med. Assoc. (JAMA), 199 (1967) 519.

51 U. Kulozik, Einflusse auf die Permeation von Wasser und gelosten Stoffen sowie auf den Deckschichtabtrag bei der Umkehrosmose, PhD Dissertation, Forschr. - Ber. VDI, Reihe 3, Nr. 120, Dusseldorf, VDI-Verlag, 1986.

52 U. Kulozik and H.G. Kessler, Effects of salt ions and deposit formation on the permeation of organic molecules in complex media in reverse osmosis, J. Membrane Sci., 54 (1990) 339-354.

53 P. Rolchigo, private communication (1991).

54 M. Lopez-Leiva, Ultrafiltration in a rotary annular filter, Ph.D. thesis, Department of Food Engineering, Lund University, Lund, Sweden (1979).

55 J. Lieberherr, Scherfiltration im Ringspalt, Ph.D. thesis, ETH, Zurich, Switzerland, 1978.

56 E. Rebsamen, Internl. Symp. Economic Optimization Strategy in Solid-Liquid Separation Processes, Louvain-La-Neuve, Belgium, (1981) 1117.

57 K.-H. Kroner, V. Nissinen and H. Ziegler, Improved dynamic filtration of microbial suspensions, Bio/Technology, 5 (1987) 921-926.

58 K.-H. Kroner and V. Nissinen, Dynamic filtration of microbial suspensions using an axially rotating filter, J. Membrane Sci., 36 (1988) 85.

59 U.B. Holeschovsky and C.L. Cooney, Quantitative description of ultrafiltration in a rotating filter device, AIChE J., 37(8) (1991) 1219-1226.

60 T. Murase, E. Iritani, P. Chidphong, K. Kano, K. Atsumi and M. Shirato, High-speed microfiltration using a rotating cylindrical, ceramic membrane, Int. Chem. Eng., 31(2) (1991) 370-378.

Appendix A

Derivation of eqn. (10) by first simplifying the Navier–Stokes equations

Assuming v_r is small, the momentum equation in the r-direction (eqn. 2a) becomes

$$\frac{\mathrm{d}p}{\mathrm{d}r}=\rho r^{-1}(v_\theta)^2 \tag{A1}$$

Substituting $v_\theta=v_\theta(r)=[\omega_o R_1^2/(R_2^2-R_1^2)][-r+R_2^2/r]$, (which is the solution to eqn. 2b when v_r is small) into eqn. (A1) and integrating from $r=R_1$ to $r=R_2$ gives

$$p(R_2)=p(R_1)-\frac{\rho\omega_o^2 R_1^4}{(R_2^2-R_1^2)^2}\left[\frac{1}{2}(R_2^2-R_1^2)-2R_2^2\log\frac{R_2}{R_1}+\frac{1}{2}R_2^4(R_1^{-2}-R_2^{-2})\right] \tag{A2}$$

We now wish to simplify the expression above in the limit that the gap size is small. Thus, we define a dimensionless parameter ϵ as $\epsilon=(R_2-R_1)/R_1$. This means $R_2=R_1(1+\epsilon)$. We need to write R_2 in the equation above for $p(R_2)$ in terms of ϵ. The term in square brackets has a non-zero leading order term proportional to ϵ^3. (The lower orders cancel.) The denominator of the coefficient multiplying the square brackets goes as ϵ^2. Thus, the lowest order approximation is linear in ϵ and looks like

$$p(R_2)=p(R_1)+\frac{\rho\omega_o^2 R_1^2}{3}\epsilon. \tag{A3}$$

This expression is essentially the modified eqn. (8). This term then remains the same in modified eqn. (10).

To get this result, we needed the polynominal and Taylor series expansions

$$R_2^2-R_1^2=R_1^2(2\epsilon+\epsilon^2) \tag{A4}$$

$$\log\,(R_2/R_1)\approx\epsilon-\frac{1}{2}\epsilon^2+\frac{1}{3}\epsilon^3 \tag{A5}$$

$$R_2^4(R_1^{-2}-R_2^{-2})=2\epsilon+5\epsilon^2+4\epsilon^3+\epsilon^4. \tag{A6}$$

Appendix B

Explicit integration of the pore construction model

$$S_1=\{2\pi\log[1+(\sigma/r^*)^2]\}^{-1/2}\int_0^\infty \exp\left\{\frac{-[\log(r\sqrt{1+(\sigma/r^*)^2}/r^*)]^2}{2\log[1+(\sigma/r^*)^2]}\right\}r^3\,\mathrm{d}r \tag{14}$$

Let $r=r^*e^u$, and $\mathrm{d}r=r^*e^u\,\mathrm{d}u$, then

$$S_1=\{2\pi\log[1+(\sigma/r^*)^2]\}^{-1/2}\int_{-\infty}^{\infty}\exp\left\{\frac{-[\log(e^u\sqrt{1+(\sigma/r^*)^2})]}{2\log[1+(\sigma/r^*)^2]}\right\}(r^*e^u)^4\mathrm{d}u$$

$$=\pi^{-1/2}\{2\log[1+(\sigma/r^*)^2]\}^{-1/2}[1+(\sigma/r^*)^2]^{-1/8}$$

$$\times \int_{-\infty}^{\infty} \exp\left[-\frac{u^2}{2\log[1+(\sigma/r^*)^2]}\right](r^*)^4 e^{7/2u} du \tag{B1}$$

Let $u = r[2\log(1+(\sigma/r^*)^2)]^{-1/2}$, and $du = [2\log(1+(\sigma/r^*)^2)]^{-1/2} dr$, then

$$S_1 = \pi^{-1/2}(r^*)^4[1+(\sigma/r^*)^2]^6 \int_{-\infty}^{\infty} \exp\left[-\left\{r - \frac{7}{4}[2\log(1+(\sigma/r^*)^2]^{-1/2}\right\}^2\right] dr$$

$$= \pi^{-1/2}(r^*)^4[1+(\sigma/r^*)^2]^6 \int_{-\infty}^{\infty} e^{-t^2} dt$$

$$= (r^*)^4[1+(\sigma/r^*)^2]^6. \tag{B2}$$

Substitute r with $(r-k)$ in eqn. (13) and then substitute into eqn. (11) with eqn. (12) gives

$$S_2 = \{2\pi\log[1+(\sigma/r^*)^2]\}^{-1/2} \int_{0}^{\infty} \exp\left\{\frac{-[\log(r\sqrt{1+(\sigma/r^*)^2}/r^*)]^2}{2\log[1+(\sigma/r^*)^2]}\right\} \frac{(r-k)^4}{r} dr \tag{B3}$$

Expand $(r-k)^4$ and solve as above, then

$$S_2 = (r^*)^4[1+(\sigma/r^*)^2]^6 - 4k(r^*)^3[1+(\sigma/r^*)^2]^3 + 6k^2(r^*)^2 - 4k^3(r^*) + k^4[1+(\sigma/r^*)^2]$$

Divide eqn. (B3) by eqn. (B2)

$$S = \frac{S_2}{S_1} = 1 - \frac{4}{q_3}\left(\frac{k}{r^*}\right) + \frac{6}{q^6}\left(\frac{k}{r^*}\right)^2 - \frac{4}{q^6}\left(\frac{k}{r^*}\right)^3 + \frac{1}{q^5}\left(\frac{k}{r^*}\right)^4 \tag{15}$$

where $q = 1 + (\sigma/r^*)^2$.

Appendix C

Estimate of the permeate centrifugal pressure on the inner surface of the membrane (*at* $r = R_1 - \bar{d}$)

In the derivation of eqn. (10) we have assumed [see above eqn. (6)] that the permeate centrifugal pressure is zero. This cannot be correct since the fluid in the permeate chamber also experiences centrifugal pressure. This error can be estimated from eqn. (2b) assuming v_r is small (i.e. $v_r = 0$) and consider the radius r in the range 0 to $R_1 - d$.

Applying the boundary conditions $v_\theta(0) = 0$ and $v_\theta(R_1 - \bar{d}) = \omega_o(R_1 - \bar{d})$, we obtain $v_\theta(r) = \omega_o r$. Then from eqn. (2a), the radial pressure is obtained from the solution of

$$\frac{dp_r}{dr} = \frac{\rho}{r} v_\theta^2 = \rho\omega_\theta^2 r \tag{C1}$$

Integrating and taking the pressure in the center to be zero, we get

$$p(R_1 - \bar{d}) = \frac{1}{2}\rho\omega_o^2(R_1 - \bar{d})^2 \tag{C2}$$

Substituting for the parameters in eqn. (C2) where $\rho = 1$ g-cm^{-3}, $\omega_o = 4000 \times 2\pi/60$ rad-sec^{-1}, $R_1 = 2.205$ cm and $\bar{d} = 0.020$ cm, we obtain $p(R_1 - \bar{d}$, 4000 rpm$) = 4.2 \times 10^{-4}$ Pa. This together with the calculated off-set pressure from eqn. (10) of $b\omega_o^2 = 0.31 \times 10^4$ Pa, we obtain 4.51×10^4 Pa which is relatively close to the measured off-set pressure of 4.6×10^4 Pa (Fig. 6a).